DFT computation, Hirshfeld surfaces analysis, non-linear optical and spectroscopic investigations of a novel non-centrosymmetric organic–inorganic hybrid material [(CH3CH2)4N]HSeO4(H2SeO4)2

Ikram Dhouib, Dhouha Abid, Ali Ouasri, Philippe Guionneau, Zakaria Elaoud

▶ **To cite this version:**

Ikram Dhouib, Dhouha Abid, Ali Ouasri, Philippe Guionneau, Zakaria Elaoud. DFT computation, Hirshfeld surfaces analysis, non-linear optical and spectroscopic investigations of a novel non-centrosymmetric organic–inorganic hybrid material [(CH3CH2)4N]HSeO4(H2SeO4)2. Journal of Solid State Chemistry, 2021, 299, 122134 (13 p.). 10.1016/j.jssc.2021.122134 . hal-03209758

HAL Id: hal-03209758
https://hal.science/hal-03209758

Submitted on 27 May 2021

HAL is a multi-disciplinary open access archive for the deposit and dissemination of scientific research documents, whether they are published or not. The documents may come from teaching and research institutions in France or abroad, or from public or private research centers.

L'archive ouverte pluridisciplinaire **HAL**, est destinée au dépôt et à la diffusion de documents scientifiques de niveau recherche, publiés ou non, émanant des établissements d'enseignement et de recherche français ou étrangers, des laboratoires publics ou privés.

DFT computation, Hirshfeld surfaces analysis, non-linear optical and spectroscopic investigations of a novel non-centrosymmetric organic – inorganic hybrid material $[(CH_3CH_2)_4N]HSeO_4(H_2SeO_4)_2$

Ikram DHOUIB[a]*, Dhouha ABID[a], Ali OUASRI[b], Philippe GUIONNEAU[c], Zakaria ELAOUD[a]

[a]*Laboratory Physical-Chemistry of Solid state, University of Sfax, Faculty of Sciences of Sfax, Tunisia.*

[b]*Laboratoire (ReSIV), Centre Régional des Métiers de l'Education et de la Formation, Madinat Al Irfane, Souissi, BP 6210 Rabat, Morocco.*

[c]*CNRS, Univ. Bordeaux, ICMCB, 87 avenue of Dr A. Schweitzer, 33608 Pessac, Bordeaux, France*

AUTHOR INFORMATION

- Corresponding author: DHOUIB Ikram
- Tel: +21697019206
- E-mail address: ikramdhouib82@yahoo.fr
- Full postal address: Sfax Faculty of Science, Chemistry Department, Soukra Road km 3,5 - B.P. 1171, 3018 Sfax – Tunisia.

Abstract

The new hybrid compound, tetraethylammonium monohydrogenselenate bis selenic acid $[(C_2H_5)_4N]HSeO_4(H_2SeO_4)_2$ is synthesized by slow evaporation at room temperature of a solution containing $(C_2H_5)_4NOH$ and H_2SeO_4. It is crystallized in the monoclinic space group Cc (Z=2), with the unit cell parameters: a = 19.705(1) Å, b = 7. 542(3) Å, c = 19.199(1) Å, β = 115°. The 3D Hirshfeld surface and 2D fingerprint plots analyses showed the predominance contribution of O-H…O bonding in the crystal structure crystal packing. The contributions importance of the different contacts in crystal packing of this compound are compared to that observed in the $[(C_3H_7)_4N]HSeO_4(H_2SeO_4)_2$ crystal. The solid-state ^{13}C NMR spectrum shows two signals corresponding to two different carbon environments in CH_2 and CH_3 groups. The IR and Raman spectra were recorded in the range 400-3600 cm^{-1} and 50-3500 cm^{-1}, respectively. The observed bands are assigned and discussed based on the theoretical analyses and computational calculated frequencies. The theoretical bond lengths, angles, and frequencies computed from the optimized molecular geometry through DFT method using B3LYP function and the 6-31G(d) basis set, are discussed and compared to the experimental results, which reveals a good agreement between the observed and calculated parameters. The nonlinear optical properties of $[(C_2H_5)_4N]HSeO_4(H_2SeO_4)_2$ were studied using the DFT method, the calculated values of the electric dipole μ, the polarizability α, and the hyperpolarizability β. The calculations showed that the selenate-based compound exhibits a non-zero b value, revealing NLO behavior which could be used in potential and functional applications including optical switching and optical disk data storage**.**

Keywords: Hybrid material, NLO response, Optical properties, Density Functional Theory (DFT), Vibrational modes, Infrared, Raman, NMR, Hirshfeld surfaces, Fingerprint plots.

1. Introduction

Over the past decades, considerable attentions have been paid in solid-state chemistry for the search and the synthesis of new class of organic-inorganic hybrid materials with low-dimensional, which may combine desirable physical-chemical properties characteristic of both organic and inorganic components within a single molecular scale composite. The hybrid compounds with quaternary ammonium cations have been found to exhibit processing and performance advantages for large area exploitation [1-4].

Particularly, several studies have been interested in hybrid compounds combining the selenate anions with organic cations [5-11]. In fact, physical properties of these hybrid compounds depend on the organic moieties and mineral acid. These materials have a non-centrosymmetric unit cell, which may reflect the possibility to obtain good materials for NLO, whereas their applications are limited due to their thermal, poor mechanical stabilities, and the lack of sufficiently large single crystals of optical quality. As a result, several reports of macroscopic and microscopic responses for organic-inorganic (NLO) systems have recently appeared in the literature [12-14]. The DFT/B3LYP-31G(d) calculated polarizability α, hyperpolarizability β, and electric dipole μ, showed good NLO properties for the $[(C_3H_7)_4N]HSeO_4(H_2SeO_4)_2$ material, crystallized in the monoclinic space group *I*a (Z = 4, a = 7.3160(2) Å, b = 31.7630(4) Å, c = 8.6890(2) Å, β = 95.340(2)°) [14]. The vibrational properties of this compound were also studied by the Infrared, Raman and RMN spectroscopy [14].

On the other hand, the single-crystal X-ray diffraction study carried out by us at room temperature showed that the $[(C_2H_5)_4N]HSeO_4(H_2SeO_4)_2$ compound crystallized in the monoclinic system with the *C*c (Z = 4) space group, and lattice parameters: a = 19.705(1) Å, b = 7.5420(3) Å, c = 19.199(1) Å, β = 115° [15]. The thermal analysis made elsewhere showed that the title compound undergone two phase transitions near 335 K and 350 K. Such results are confirmed through electrical and dielectric measurements, which revealed the relaxation phenomenon and a super-protonic conduction for this material [15].

The present paper aims to complete the previous study made on $[(C_2H_5)_4N]HSeO_4(H_2SeO_4)_2$ compound by analyzing the Infrared, Raman and RMN spectra, constructing Hirshfeld surfaces, and calculating the NLO properties for this compound. The vibrational modes factor group analysis and the calculated frequencies of $[(C_2H_5)_4N]HSeO_4(H_2SeO_4)_2$ compound are developed and compared to the results found for $[(C_3H_7)_4N]HSeO_4(H_2SeO_4)_2$ crystal. So, the geometric parameters and vibrational frequencies

have been investigated by the DFT/B3LYP/6-31G(d) method, which was performed in terms of comparison with the structural study carried out elsewhere. The non-linear optical properties of the title compound are studied theoretically, which allowed us to calculate the electric dipole moment μ_{tot}, the isotropic polarizability α_{tot}, and the first hyperpolarizability β_{tot}. The solid CP-MAS ^{13}C NMR characterization is also discussed.

2. Materials and Methods

Crystal of $[(C_2H_5)_4N]HSeO_4(H_2SeO_4)_2$ was prepared by slow evaporation technique, at room temperature, from an aqueous solution containing selenic acid and tetraethylammonium hydroxide in the stoichiometric ratio 3:1. This mixture was stirred well till it became clear. Over a period of several days, colorless parallelepipedic crystals with high quality suitable for X-ray single crystal experiments were obtained. The reaction scheme is given in the following equation:

$$(C_2H_5)_4NOH + 3H_2SeO_4 \longrightarrow [(C_2H_5)_4N]HSeO_4(H_2SeO_4)_2 + H_2O$$

2. 1. Spectroscopic measurements

The vibrational measurements were carried out at room temperature. The infrared absorption spectrum of $[(C_2H_5)_4N]HSeO_4(H_2SeO_4)_2$ was recorded in the range 4000-400 cm^{-1} on a PERKIN-ELMER FT-IR spectrometer. The sample were diluted with spectroscopic grade KBr and pressed into a pellet, with a spectral resolution of 2 cm^{-1}. The Raman spectrum of this compound was recorded using Horiba Jobin Yvon LabRAM HR 800 Dual Spectrophotometer. The excitation line was the 630 nm from a Neon laser in the range 0-4000 cm^{-1}. The laser beam was focused on the sample through a 50×LF objective microscope and the incident power was limited to 5 mW to avoid sample heating degradation.

The NMR–magic-angle spinning (MAS) experiments have been done at room temperature on a Bruker WB 7.05 Tesla. Then, the powdered sample was wrapped in a 4 mm diameter rotor and set to rotate at a speed up to 8 kHz in a Doty MAS probe head. The ^{13}C spectrum was collected by a cross-polarization of the proton with 15.6 μs contact time.

2 .2. Theoretical calculations

The geometry was fully optimized without any constraint with the help of analytical gradient procedure implemented within Gaussian 03 program [16]. All parameters were allowed to relax and the calculations were converged to an optimized geometry which corresponds to a true energy minimum revealed by the lack of imaginary values in the wavenumber calculations. Vibrational frequencies were calculated with B3LYP/6-31G(d).

2.3. Hirshfeld surfaces method

The 3D molecular Hirshfeld surfaces may be constructed using Crystal Explorer package [17], which accepts the file format, by dividing space in the crystal into regions, where the electron distribution of a sum of atoms for the molecule dominates the corresponding sum over the crystal [18-19]. The Hirshfeld surface is characterised with two distances: d_i, from the Hirshfeld surface to the nearest nucleus inside the surface, and d_e, to the nearest nucleus outside the surface. The normalized contact distance d_{norm} is defined in terms of di, de, and the van der Waals radii of the atoms, as: $\mathbf{d_{norm}} = \frac{\mathbf{d_i} - \mathbf{r_i^{vdW}}}{\mathbf{r_i^{vdW}}} + \frac{\mathbf{d_e} - \mathbf{r_e^{vdW}}}{\mathbf{r_e^{vdW}}}$, with r_i^{vdW} and r_e^{vdW}, are the appropriate atoms' van der Waals radii, being internal and external to the surface, respectively. The 2D fingerprint plots obtained by d_{norm} Hirshfeld surface identify quantitatively the relative contribution of each intermolecular interaction on the surfaces' area, and illustrate the fingerprint map of $atoms_{inside}/atoms_{outside}$ molecules' interactions [17, 20, 21]. The acceptor atoms in the interactions are shown with negative electrostatic potentials (red regions), and donor atoms are shown with positive electrostatic potentials (blue regions) [22].

3. Results and discussion

3.1. Structural and DFT analyses

The $[(C_2H_5)_4N]HSeO_4(H_2SeO_4)$ compound crystallized in the monoclinic *C*c (Z=4) space group [a = 19.705(1) Å, b = 7.542(3) Å, c = 19.199(1) Å, β = 115°, V = 2181.9(2) A°^{3}] [15], with the unique axis b. The asymmetric unit of the compound crystal structure, presented in Figure 1(a), contains one organic cation $[(C_2H_5)N]^+$, two types of selenate species with different ionization state: a monoanion $[HSeO_4]^-$ and two H_2SeO_4 acid molecules, It is worthy to notice that all atoms are located in general positions, corresponding to the Wyckoff positions (4a) of the Cc space group. Figures 2 and 3 represents the atomic arrangement of the structure which reveals a layered arrangement of organic and in organic groups along the b axis. The mid-planes of the tetraethylammonium groups are located at x = 0 and x = 1/2. In the $[(C_3H_7)_4N]HSeO_4(H_2SeO_4)_2$ compound, monoclinic of *I*a (Z=4) space group [a = 7.3160(2) Å, b = 31.7630(4) Å, c = 8.6890(2) Å, β = 95.340(2)°, V = 2010.37(8) A°^{3}] [14], the propylammonium chains, parallel to the b-direction, were located at x =0 and z =1/2. It is

mentioning that the *I*a (Z=4) space group is one of the non-standard space groups of *C*c (Z=4), obtained by the (a, b, c) to (c, b, -a-c) matrices transformation.

The selenate inorganic groups in $[(C_2H_5)_4N]HSeO_4(H_2SeO_4)_2$ are interconnected to each others through strong O-H…O hydrogen bond, yielding infinite 2D chains built up through $[(HSeO_4)(H_2SeO_4)]_n^{n-}$ layers perpendicular to the a-axis, and alternating with the $^{+}N(C_2H_5)_4$ organic groups planes. The mid-planes of the selenate layers are located at x = 1/4 and x = 3/4 (Figure 3). In contrast, for the $[(C_3H_7)_4N]HSeO_4(H_2SeO_4)_2$ material, the selenate inorganic layers were built up by infinite chains of $[(H_2SeO_4)_2HSeO_4]^{n-}{}_n$ anions parallel to the b-direction [14]; while, the midplanes of the selenates groups, are located at z =1/4 and z =3/4.

The d(D…A) hydrogen bonding vary in 2.480(16) - 2.788(19) Å for $[(C_2H_5)_4N]HSeO_4(H_2SeO_4)_2$ [15], and in 2.29(2) - 2.42(2) Å in $[(C_3H_7)_4N]HSeO_4(H_2SeO_4)_2$ [14], indicating that that the hydrogen bonding are more strong in the compound containing the terapropylammonium cations. Even if the tetrapropylammonium are voluminous than the tetraethylammonium cations, one can state that the unit cell volume ($A°^3$) [2010.37(8)] of $[(C_3H_7)_4N]HSeO_4(H_2SeO_4)_2$ is small than that found for $[(C_2H_5)_4N]HSeO_4(H_2SeO_4)_2$ [2181.9(2)]. This may be explained by the strong hydrogen bonds observed in the compound with terapropylammonium cations, which could affect the unit cell volume. More informations on the importance of hydrogen bonding in these two compounds is discussed in the Hirshfeld surfaces part.

The optimized molecular geometry of $[(C_2H_5)_4N]HSeO_4(H_2SeO_4)_2$ compound, illustrated in Figure 1(b), was carried out for the inorganic units ($[HSeO_4]^-$ and H_2SeO_4) and organic cation $[(C_2H_5)N]^+$ using DFT/B3LYP/6-31G(d) basis set. The selected measured bond lengths and angles with the calculated ones are presented in Tables 1 and 2, in accordance with the atom numbering scheme given in Fig. 1(a). A comparative study between the two geometries shows that the mean absolute difference order between experimental and optimized values are of 0.027 Å and 0.041° for inter-atomic bond lengths and for angles, respectively. In fact, the small deviation between the calculated and experimental values is not surprising since the theoretical calculations were developed based on the isolated molecule, considered as in the gaseous phase at 0 K, while the experimental X-Ray results belong to the molecules in the solid-state with inter-molecular interactions and crystal packing effect.

The correlation diagrams between the calculated and experimental geometric parameters are carried out (Fig 4), and the correlation coefficients calculated through the linear fits of the curves are 0.99336 and 0.97762 for bond lengths and angles, respectively.

These results indicate that the calculation precision is satisfactory, and the B3LYP/6-31G(d) level is suitable for the complex system studied here.

3.2. Hirshfeld surfaces analyses

The $[(C_2H_5)_4N]HSeO_4(H_2SeO_4)_2$ crystal structure packing is quantified with Hirshfeld surface analysis (3D) and fingerprint plots (2D) using Crystal Explorer package [17]. The Hirshfeld surfaces are particularly mapped with the conventional mapping d_{norm} (figure 5.a); the inter-contacts may be negative or positive value since the intermolecular contacts may be shorter (red color) or longer (blue color) than van der Waals separations. The contacts being equal to the sum of van der Waals radii are showed in white.

The circular depressions shown as relatively deep red spots in d_{norm} surface (figure 5.a), indicate the presence of close-contact interactions, due mainly to O-H···O hydrogen bonding. These contacts are highlighted in the Hirshfeld surface plot by the relatively bright red spots area. All intermolecular interactions contribution (100%) in the $[(C_2H_5)_4N]HSeO_4(H_2SeO_4)_2$ crystal packing are provided quantitatively by resolving the 3D d_{norm} surface (figure 5.a) into 2D fingerprint plots (figure 6 a-d), which illustrate the different interactions contribution to the total Hirshfeld surfaces, commonly overlapped in the full 2D fingerprint plots (Figure 5.b). The percentage of area occupied by different interactions (O···H/H···O, H···H/H···H, O···O/O···O, Se-H/H···Se) in the crystal packing is given in the figure 6 (a-d).

The prominent regions observed in the fingerprint plots (figure 6-a), where a molecule acts as an acceptor ($d_e>d_i$) and as a donor ($d_e<d_i$), correspond to the O···H/H···O interactions showed by two spikes: one in the bottom left area (donor) at ($d_e \cong 1$ Å, $d_i \cong 0.68$ Å), and the other at ($d_e \cong 0.68$ Å, $d_i \cong 1$ Å) in the bottom right (acceptor). These important contacts (69.8%) of the crystal packing are indicative of strong O-H···O hydrogen bonding in the $[(C_2H_5)_4N]HSeO_4(H_2SeO_4)_2$ compound.

The H···H/H···H contacts (Figure 6-b) appeared in the scattered points middle of the 2D fingerprint plot along with an appreciable peak is observed at ($d_e \cong 1.2$Å, $d_i \cong 1.2$ Å) ; these contacts representing 25.4% of the entire Hirshfeld surfaces are considered as relatively important in the title crystal packing. The O···O/O···O contacts covering 4.6 % of the total crystal surface (Figure 6-c) are considered as the third important contributor in the crystal packing. At last, the Se···H/H···Se intercontacts are found to occupy a very weak area of the total surfaces (0.1 %) as presented in the Figure 6-d.

The major contribution of O···H/H···O in the total surface highlight the O-H···O hydrogen bonding importance in the $[(C_2H_5)_4N]HSeO_4(H_2SeO_4)_2$ crystal packing, which is in

well agreement with the X-ray results, concerning the effect of hydrogen bonding in the crystal cohesion of the title compound [15].

To compare the tetraethylammonium crystal packing to that of terapropylammonium [14], the Hirshfeld surfaces and fingerprint plots mapped with d_{norm} are constructed for the $[(C_3H_7)_4N]HSeO_4(H_2SeO_4)_2$ compound, as presented in the figures 7 and 8. Indeed, The prominent regions observed in the fingerprint plots (figure 7-a) correspond to the O···H/H···O interactions showed by two spikes: the donor in the bottom left area ($d_e \cong 0.92$ Å, $d_i \cong 0.54$ Å), and the acceptor in the bottom right ($d_e \cong 0.54$ Å, $d_i \cong 0.92$ Å). These contacts, indicating the importance of the O-H···O hydrogen bonding, present 56 % of the crystal packing of the $[(C_3H_7)_4N]HSeO_4(H_2SeO_4)_2$ compound. The H···H/H···H contacts (Figure 8-b) characterized by an appreciable fingerprint peak at ($d_e \cong 1.05$ Å, $d_i \cong 1.05$ Å) represent 36 % of the entire Hirshfeld surfaces. The O···O/O···O contacts cover 7.6% of the total crystal surface (Figure 8-c), while the Se···H/H···Se intercontacts occupy a very weak area of the total surfaces (0.1%) as presented in the Figure 8-d.

The table 3 illustrates the percentage contributions of the different contacts in the crystal packing of the two selenate compounds, with the characteristic d_e and di distances observed for the important contacts O….H/H…O, H….H/H…H, and O...O/O…O. As stated, all donor (de, di) and acceptor (de, di) distances of $[(C_3H_7)_4N]HSeO_4(H_2SeO_4)_2$ compound are small than that observed in the $[(C_3H_7)_4N]HSeO_4(H_2SeO_4)_2$ compound, which is compatible with the fact that the unit volume of the terapropylammonium selenate is small than the unit volume of the tetraethylammonium selenate .

3.3. Hyperpolarizability calculation

The polarization phenomenon is due to an induced dipole moment, which is created by an external electric field under an intense electric field. Taylor series expansion has been used to demonstrate the material total energy U, given by the following relationship:

$$U(\vec{E}) = U(0) - \sum_i \mu_i E_i - \frac{1}{2!}\sum_{ij} \alpha_{ij} E_i E_j - \frac{1}{3!}\sum_{ijk} \beta_{ijk} E_i E_j E_k - \cdots$$

Where the i, j, k subscripts represent the different components of x, y, z Cartesian coordinates system, U(0) is the energy of the compound in the absence of E , μ_i is the molecular permanent electric dipole moment along the i^{th} direction, E_i is the i^{th} Cartesian component of the applied electric field E, α is the linear polarizability, and β is the first order

hyperpolarizability. The μ_{tot}, α_{tot} and β_{tot} magnitudes are calculated using the following equations [23]:

$$\mu_{tot} = \sqrt{(\mu_x^2 + \mu_y^2 + \mu_z^2)}$$

$$\alpha_{tot} = \frac{\alpha_{xx} + \alpha_{yy} + \alpha_{zz}}{3}$$

$$\beta_{tot} = \sqrt{(\beta_x^2 + \beta_y^2 + \beta_z^2)}$$

Where:

$$\beta_x^2 = (\beta_{xxx} + \beta_{xyy} + \beta_{xzz})^2$$

$$\beta_y^2 = (\beta_{yyy} + \beta_{yzz} + \beta_{yxx})^2$$

$$\beta_z^2 = (\beta_{zzz} + \beta_{zxx} + \beta_{zyy})^2$$

Since the values of the polarizability α_{tot} and the first hyperpolarizability β_{tot} of Gaussian 03 output are reported in atomic units (a.u), the calculated values have been converted into electrostatic units (esu) (1 a.u = 0.1482×10^{-24} esu: 1 a.u = 8.6393×10^{-31} esu).

The Table 4 lists the B3LYP/6-31G(d) results of the electronic dipole moment (i = x, y, z), the polarizability, and the first hyperpolarizability for the $[(C_2H_5)_4N]HSeO_4(H_2SeO_4)_2$. The calculated dipole moment is equal to 13.4084D (Debay). The high value of dipole moment is observed for μ_x component at 12.6018D; for the y and z directions, these values are equal to -4.2282 D and 1.7615 D respectively. For the $[(C_3H_7)_4N]HSeO_4(H_2SeO_4)_2$ compound [14], the highest dipole moment value was observed for the μ_z component (12.8146D), while μ_x and μ_y values were calculated at 0.1703D and -2.2407D, respectively. The transformation of the high value of dipole moment from the a direction to the c direction is in well agreement with the space groups notation *I*a and *C*c assigned to $[(C_2H_5)_4N]HSeO_4(H_2SeO_4)_2$ and $[(C_3H_7)_4N]HSeO_4(H_2SeO_4)_2$, respectively. The calculated polarizability α_{tot}, is equal to zero esu in the studied tetraethylammonium compound, against the 32.99×10^{-24} esu value calculated for $[(C_3H_7)_4N]HSeO_4(H_2SeO_4)_2$, compound [14].

The first hyperpolarizability β_{tot} of the material is calculated at the 16.154×10^{-31} esu value, which is about 2.35 times more than that of the reference crystal KDP (β_{KDP} = 6.85×10^{-31} eus). This value represents about the half of the calculated value for the compound

containing terapropylammonium cations (β = 31.05×10^{-31} eus) [14]. The large β value calculated by the DFT/B3LYP/6-31G(d) confirms that the tetraethylammonium material is a good candidate for NLO applications, but less than the compound with the terapropylammonium cations considered as possessing more good NLO properties [14]. As has been stated, the first hyperpolarizability β_{tot} value is of 100.47×10^{-31} eus of $[(C_3H_7)_4N]H_2AsO_4(H_3AsO_4)_2$ [12], which is about 14.6 times more than that of the reference crystal KDP. Hence, we can admit that the first hyperpolarizability β_{tot} increases when passing from tetraethylammonium to more voluminous terapropylammonium cations in the selenate compounds. For the terapropylammonium compounds, it seems that the first β_{tot} increases strongly by the substitution of the selenate [14] anions by the arsenate ones [12].

3.4. NMR spectroscopy

The experimental spectrogram of high resolution nuclear magnetic resonance of the ^{13}C MAS NMR is reported for the $[(C_2H_5)_4N]HSeO_4(H_2SeO_4)_2$ salt in Figure 9. The ^{13}C NMR spectrum presents two signals for three different carbon environments. The first signal observed at about 9.51 ppm corresponds to CH_3 groups of tetraethylammonium cations; the corresponding peak was observed at 8.31 ppm for the compound with terapropylammonium cations $[(C_3H_7)_4N]HSeO_4(H_2SeO_4)_2$ [14]. So, the CH_3 signal is shifting to the high frequencies in the compound containing tetraethylammonium cations. The second signal assigned to the CH_2 carbon groups is located approximately at 54.97 ppm, with little shifting at low frequencies compared to the 55.47 ppm value observed in the compound with Tetrapropylammonium cations [14]. The presence of these peaks suggests the presence of two types of carbon atoms, which confirms the results of the structural resolution and the purity of the crystalline phase of the product. These results are compared to some works which contain these different groups CH_3 and CH_2 [14, 24].

3. 5. Vibrational studies of $[(C_2H_5)_4N]HSeO_4(H_2SeO_4)_2$

3.5.1. Vibrational modes analysis of $(CH_3CH_2)_4N^+$ cations

The free tetraethylammonium cation considered in D_{2d} symmetry posses 81 internal vibrational modes, described as: 12 A_1 (Ra) + 8A_2 (IR) + 9 B_1 (Ra) + 12 B_2 (IR) + 20 E (IR, Ra) [25-26]. Inside the $N(C_2H_5)_4HSeO_4(H_2SeO_4)_2$ crystal structure (space group Cc, Z=4), the $(CH_3CH_2)_4N^+$ cations were placed in positions generals [15], i.e. in the sites of C_1 symmetry. By lowering symmetry from D_{2d} to C_1, the 81 vibrational modes of the cations become of A

symmetry compatibly to the site group given in the Table 5. Each of these vibrations should split into two components in the group factor C_s, giving (81A', 81B") modes, all Raman and Infrared active in the factor group of the crystal. As predicted by the theoretical group analysis, the tetraethylammonium cationic modes could be observed as well as in Raman and Infrared spectra. The assignment of these modes is made in comparison to the compounds containing similar tetraalkylammonium cations, studied elsewhere **[**25-31**]**.

3.5.2. Vibrational modes analysis of $[HSeO_4]^-$ and H_2SeO_4

The free $[SeO_4]^{2-}$ anion considered in T_d symmetry has 9 internal vibrational modes: A_1 (Ra) + E (Ra) + $2F_2$ (Ra, IR), which correspond to two stretching modes ν_1(A_1: ν_s Se-O), ν_3 (F_2: ν_{as} Se-O), and two bending modes ν_2 (E: δ_s O-Se-O), ν_4 (F_2: δ_{as} O-Se-O) [31]. The ν_1 (A_1) and ν_2 (E) modes actives in Raman appeared around 837 cm^{-1} and 345 cm^{-1}, respectively; while the ν_3 (F_2) and ν_4 (F_2), too Raman and Infrared actives, appeared near 873 cm^{-1} and 413 cm^{-1}, respectively [10].

The free H_2SeO_4 and $[HSeO_4]^-$ groups are considered in C_{2v} and C_{3v} symmetry, respectively [14]. In the crystal, these species were too placed in the general positions [15], corresponding to the (C_1) sites symmetry of the space group *C*c. Among the 15 internal modes of H_2SeO_4 described in C_{2v} symmetry ($6A_1 + 4B_1 + 2A_2 + 3B_2$), nine are corresponding to the vibrational modes ($A_1 + E + 2F_2$) of the free $[SeO_4]^{2-}$ considered in T_d symmetry, and 6 vibrations ($4A_1 + 2B_1$) corresponding to OH vibrations of H_2SeO_4 in C_{2v} symmetry [14].

By lowering symmetry of H_2SeO_4 from C_{2v} to C_1, the site symmetry correlations lead to 15 modes of A symmetry, among them 9 modes are due to the $[SeO_4]^{2-}$ anion, and 6 modes are due to OH groups of H_2SeO_4 (Table 6). For $[HSeO_4]^-$, among the 12 internal modes ($4A_1 + 2A_2 + 3E$) described in C_{3v} symmetry, nine ($3A_1 + 3E$) are due to the vibrational modes of the tetrahedral $[SeO_4]^{2-}$ of T_d symmetry, and three ($A_1 + 2A_2$) are due to the OH vibrations of $[HSeO_4]^-$ of C_{3v} symmetry. The site symmetry approach (Table 7) leads to 12 vibrational modes of A symmetry, which are due to nine (A) modes of the $[HSeO_4]^-$ and three vibrations (A) of OH group associated to the $[HSeO_4]^-$.

At last, the $[(H_2SeO_4)_2HSeO_4]^-$ vibrational modes representation given in the Table 7 predicts 27 (A) vibrational modes originated from $[SeO_4]^{2-}$ groups ($5A_1 + 5E + 4F_2$), and 15

(A) modes due to OH groups of H_2SeO_4 and $[HSeO_4]^-$. All these modes should be active as well as in Raman and Infrared spectra.

3.5.3. Infrared and Raman spectra interpretation

The Infrared and Raman spectra recorded at room temperature for the compound $N(C_2H_5)_4HSeO_4(H_2SeO_4)_2$, and those calculated by the DFT computational method, are given in the Figures 10 and 11, respectively. The assignment of the observed bands to the relative vibrational modes is made based on the theoretical group analysis predicting the tetraethylammonium and selenate species vibrational modes, which could be Raman and Infrared active in the title crystal (Tables 5-9). The bands assignment is compared as well to the density functional theory DFT (B3LYP/6-31G(d)) frequencies calculations results, and to the previous results made on similar compounds [10, 14, 25-32]. The Table 9 shows the experimental and theoretical frequencies assignment to their corresponding vibrational modes.

* Hydrogen bonding vibrations (3100-3850 cm^{-1})

In this region of the IR and Raman spectra of the title compound, appeared several bands of weak to strong intensities, as given in the Table 9. A rigorous assignment of these bands is more difficult, because of two types of OH vibrational modes are involved in this region: the ν(OH…O) modes due to the hydrogen bonding taken place in the crystal [15], and the stretching modes ν(OH) of the selenate $[HSeO_4]^-$ and H_2SeO_4 species, being not implied in the hydrogen bonding [24]. An attempt of the assignment of these bands is made based on previous works reporting this type of compounds [14, 24].

In the Infrared spectrum, several bands of weak intensities are observed between 3995 and 3500 cm^{-1} (Figure 10, Table 9), which could be due to the ν (Se-OH) stretching modes. In the Raman spectrum, only two bands observed at 3875 and 3850 cm^{-1} may be originated by the modes. The ν(Se-OH) are rarely observed in the literature above 3700 cm^{-1} [14]. To note that harmonic modes may be observed in this spectral region, when strong vibrational bands are observed near 1400 cm^{-1}, which is not well stated as well as in the Infrared and Raman spectra of the title compound. Hence, the assumption assigning the observed band above 3700 cm^{-1} to the ν (Se-OH) stretching modes appeared as the most logic.

* Tetraethylammonium cationic vibrations (3100- 400 cm^{-1})

In the C-H spectral region (2800-3100 cm^{-1}), the Raman spectrum presents only a weak band at 3025 cm^{-1}, which is assigned to the asymmetric stretching modes $\nu_{as}(CH_2)/\nu_{as}(CH_3)$;

these modes give rise in the Infrared spectrum to three bands of weak intensities at 3030 and 3000 cm^{-1}. The symmetric stretching modes $\nu_s(CH_2)/\nu_s(CH_3)$ not observable in the Raman spectrum, give however a medium Infrared band at 2937 cm^{-1}. Between 2900 and 2800 cm^{-1}, the Infrared spectrum presents one medium band at 2863 cm^{-1} and another weak/broad feature at 2800 cm^{-1}, while the Raman spectrum did not present any band in this region. The assignment of the observed Infrared bands in this region is not easy and definitive; so, the band at 2863 cm^{-1} could be due to the $\nu_s(CH_2)/\nu_s(CH_3)$ modes, and (or) to ν (O-H....O) modes involving hydrogen bonding effect in this compound [14, 32]. The weak band with frequency at 2800 cm^{-1} may be due to ν (O-H....O) modes or to the non-fundamental modes [28].

In the spectral region spreading below 2800 cm^{-1}, the Raman bands of medium intensities observed at 1935, 1908, 1860 cm^{-1}, and the weak band at 1772 cm^{-1} are assigned undoubtedly to non-fundamental modes as has been found for several compounds containing hydrogen bonding [14, 32]. The DFT calculated frequencies in this region are 1930, 1892, 1881, and 1770 cm^{-1}, which is considered in sufficient agreement with the observed Raman bands. To note that the hydrogen bonding of O-H....O type, varying from 1.86 Å to 2 Å for H....O bond lengths, have been determined by the X-Ray study made recently on the title compound [15]. The importance of O-H....O hydrogen bonding in the title compound is quantitatively highlighted from the Hirshfeld surface analysis (Figure 6.a), in well agreement with the structural and vibrational results.

The Infrared bands observed at 1516 and 1453 cm^{-1} are assigned to the asymmetric bending modes $\delta_{as}(CH_3)$ and $\delta_{as}(CH_2)$, which are not observed in the Raman spectrum. The band at 1516 cm^{-1} could be due to "in-plane bending" δ (Se-OH) modes. The symmetric bending modes $\delta_s(CH_3)/\delta_s(CH_2)$ give in the Infrared spectrum one medium band at 1410 cm^{-1} in well compatibility with the calculated frequency (1412 cm^{-1}) of these modes, and in the Raman spectrum two weak bands at 1410 and 1326 cm^{-1}.

The twisting modes $t(CH_2)$ give rise, in the Raman spectrum, to one medium band at 1326 cm^{-1} and to another weak band at 1305 cm^{-1}. In the Infrared spectrum, these modes are observed as a band of medium intensity at 1305 cm^{-1}. The Infrared and Raman frequencies of 1350 may be due either to the selenate δ (Se-OH) modes. Hence, the observation of the δ(Se-OH) modes over this spectral region makes more difficult the assignment of $\delta(CH_3)/\delta(CH_2)$ and $t(CH_2)$ modes, as has been found generally in the type of compounds.

The rocking ρ_r (CH_3) and the skeletal stretching modes [ν(C-N), ν(C-C)] modes are observed in the two vibrational spectra of this compound over the spectral range (1250 - 400

cm^{-1}) as illustrated in the Table 9. A rigorous assignment of the bands observed in this region is either not easy, due to the appearance of the "out-of-plane bending" γ (Se-OH) modes and the internal modes of the $[HSeO_4]^-$ and H_2SeO_4 species over this spectral region.

* Selenate species vibrations (3900-50 cm^{-1})

The selenate asymmetric stretching modes ν_3 [ν_{as} (Se-O)] are observed as two medium Infrared bands at 947 and 905 cm^{-1}; these modes give a medium band in the Raman spectrum at 847 cm^{-1}. The band of weak intensity observed in the Raman spectrum at 842 cm^{-1} is assigned to the symmetric stretching mode ν_1 [ν_s (Se-O)]. The symmetric vibrational modes ν_1 (A_1) are not observed in the Infrared spectrum in the corresponding frequency range, as expected for H_2SeO_4 in C_{2v} symmetry (Table 6) and for $[HSeO_4]^-$ in C_{3v} symmetry (Table 6). So, the ν_1 (A_1) modes are only Raman active as expected in the $[SeO_4]^{2-}$ in the T_d symmetry.

The internal vibrational modes of the hydrogen selenate species H_2SeO_4 and $[HSeO_4]^-$ are found to be considerably different from those due to the "isolated" selenate $[SeO_4]^{2-}$ anion. Indeed, the medium Raman bands appeared at around 800 and 748 cm^{-1} may be due to the stretching modes ν(Se–OH) of the longest Se-OH bonds taken place in the $[HSeO_4]^-$ and H_2SeO_4 species, which are considered as two components of the ν_3 (ν_{as}: Se-O) modes [32].

The band of weak intensity observed in the infrared spectrum at 453 cm^{-1} and the four weak bands observed in the Raman spectrum at 516, 463, 421 and 400 cm^{-1} are assigned to the asymmetric bending modes ν_4 (δ_{as}: O-Se-O). The observation of four Raman components in this region may be due to the degenerate modes ν_4 (F_2) splitting under the site symmetry effect C_1, which indicates the selenate species $[HSeO_4]^-$ and H_2SeO_4 distortion in the title compound. The symmetric ν_2 (δ_s: O-Se-O) mode, already Infrared inactive in the $[SeO_4]^{2-}$ anion of T_d symmetry, is observed as a weak band in the Raman spectrum at 274 cm^{-1}; the frequency of the ν_2 (E) $[SeO_4]^{2-}$ selenate vibrations are here shifted from its known region (320-340 cm^{-1}) as given in the literature for [10, 32]. The "out-of-plane bending" γ (Se-OH) modes coming from the H_2SeO_4 and $[HSeO_4]^-$ species are observed in the Infrared spectrum as two strong bands at 1053 and 1030 cm^{-1}, and a weak band at 1105 cm^{-1}. In the Raman spectrum, these modes appeared as a medium band at 1053 cm^{-1}, and two weak features at 1095 and 1010 cm^{-1}. For the in-plane bending δ (Se-OH) vibrational modes of the selenate species, they are observed as medium to strong Infrared bands at 1684, 1642, 1600 cm^{-1}; these modes appeared as weak features in the Raman spectrum at 1686, 1654 and 1600 cm^{-1}. The

δ(Se-OH) modes may be also the origin of the weak and medium Infrared bands appeared at 1516 and 1305 cm^{-1}.

In the Raman spectrum of the title compound, the strong band appeared at 105 cm^{-1} and the two weak features observed at 63 and 42 cm^{-1} are considered as external vibrational modes (lattice modes). The observation of a strong intensity of the mode observed at 105 cm^{-1} implied important rotational motions in the title compound, which could affect the neighbouring internal vibrational modes ν_2 (δ_s: O-Se-O) of H_2SeO_4 and $[HSeO_4]^-$ species, observed here at lower frequency of in its known region (320-350 cm^{-1}).

For all characteristic spectral regions, the calculated frequencies are considered generally in sufficient agreement with the observed Infrared ad Raman frequencies (Table 9), which more support the assignment purposed in this work.

4. Conclusions

The $[(C_2H_5)_4N]HSeO_4(H_2SeO_4)_2$ compound was synthesized by slow evaporation at room temperature of an aqueous solution containing $N(C_2H_5)_4OH$ and H_2SeO_4. The X-ray single crystal diffraction study showed that the title compound crystallized in the non-centrosymmetric space group *C*c (Z=4). Its structure consists of an infinite two-dimensional layers $[(HSeO_4)(H_2SeO_4)]_n^{n-}$ in which the $(HSeO_4)^-$ and H_2SeO_4 tetrahedra are linked by O–H…O hydrogen bonds.

The Hirshfeld surface and fingerprint plots analyses showed that O···H/H···O inter contacts due to O-H···O hydrogen bonding have the major contribution in the total surface of the crystal packing, in agreement with X-ray and spectroscopy results indicating the existence of strong hydrogen bonding in the $[(C_2H_5)_4N]HSeO_4(H_2SeO_4)_2$ compound. The contributions importance of the different contacts in this compound are compared to that observed in the $[(C_3H_7)_4N]HSeO_4(H_2SeO_4)_2$ crystal.

The calculated first hyperpolarizability β_{tot} is about 2.35 times of the reference crystal KDP (β_{KDP} = 6.85×10^{-31} eus), indicating that the title hybrid compound is an interesting future material with nonlinear optical properties.

The chemical shift undergone through ^{13}C in the NMR spectrum confirms the presence of two types of carbon hybridation ($-CH_2$, $-CH_3$) in the $[(C_2H_5)_4N]HSeO_4(H_2SeO_4)_2$ structure.

The IR and Raman active modes of $C_2H_5)_4N^+$, $(HSeO_4)^-$ and H_2SeO_4 determined in the crystal using theoretical group analyses, and the observed frequencies efficiently compared to

that calculated by the DFT method, support the interpretation of the bands observed in the vibrational spectra of the title compound.

Finally, we believe that these results appear to be very interesting route to enrich knowledge on the crystal structure and physical properties of hybrid materials and should be useful to improve their performance for interesting applications in electronic devices, optical computers and optical signal processing**.**

Conflicts of interest

The authors declare no competing financial interest.

Reference

[1] G. Yang, H.G. Zhu, B.H. Liang, X.M. Chen, J. Chem. Soc. Dalton Trans. 5 (2001) 580.

[2] Z. Wang, D. Xie, F. Zhang, J. Yu, X. Chen, C. Ping Wong, Science Advances. 6 (48) (2020).

[3] X. Liu, W. Xu, S. Xu, X. Yu, Y. Deng, X. Wu, F. Liang, Q. Wu, Inorganic Chemistry. 59 (8) **(**2020) 5721.

[4] W. Trigui, F. Hlel, RSC Advances. 9 (2019) 24291.

[5] W. Maalej, A. Ben Rached, T. Mhiri, A. Daoud, N. Zouari, Z. Elaoud. Journal of Physics and Chemistry of Solids. 96 (2016) 92

[6] M. Fleck, Journal of Acta Crystallogr E. 62 (2006) 4939.

[7] M. Drozd, J. Baran, Journal of Spectrochimica Acta Part A. 61 (2005) 2953.

[8] M. Drozd, J. Baran, A. Pietraszko, Journal of Spectrochimica Acta Part A. 61 (2005) 2775.

[9] A. Pawlowski, B. Hilczer, M. Polomska, A. Pietraszko, Journal of Solid State Ionic. 145 (2001) 217.

[10] J. Baran, M. S´ ledz´, M. Drozd, A. Pietraszko, A. Haznar, H. Ratajczak, Journal of Molecular Structure. 526 (2000) 361.

[11] B. Hilczer, M. Polomska, A. Pawlowski, Journal of Solid State Ionic. 125 (1999) 163

[12] I. Dhouib, H. Feki, P. Guionneau, T. Mhiri, Z. Elaoud. Journal of Spectrochimica Acta. A 131 (2014) 274.

[13] I. Dhouib, P. Guionneau, Z. Elaoud, Journal of Coordination Chemistry. 70 (2017) 3585.

[14] I. Dhouib, A. Ouasri, P. Guionneau, S. Pechev, Z. Elaoud, Journal of Chemical Saudi Society. 24 (2020) 996-1009.

[15] D. Abid, I. Dhouib, P. Guionneau, S. Pechev, I. Chaabane, N. Daro, Z. Elaoud, Journal of Alloys and Compounds. 824 (2020) 153826.

[16] M.J. Frish, G.W. Trucks, H.B. Schlegel, G.E. Scuseria, M.A. Robb, J.R.Cheeseman, V.G. Zakrzewski, J.A. Montgomery, J.R.E. Stramann, J.C.Burant, S. Dapprich, J.M. Millam, A.D. Daniels, K.N. Kudin, M.C. Stain, O. Farkas, J. Tomasi, V. Barone, M. Cossi, R. Cammi, B. Mennucci, C.Pomelli, C. Adamo, S. Clifford, J. Ochterski, G.A. Petersson, P.Y. Agula, Q. Cui, K. Morkuma, D.K. Malick, A.D. Rabuck, K. Raghavachri, J.B.Foresman, J. Cioslowski, J.V. Ortiz, A.G. Baboul, B.B. Stefanov, G. Liv, A. Liashenko, P. Piskorz, I.Komaromi, R. Comperts, R.L. Martin, D.J. Fox, T. Keith, M.A. Al-Laham, C.Y. Peng, A. Nanayakkaray, M. Challacombe, P.M.W. Gill, B. Johnson,W. Chen, M.W.Wang, J.L. Andres, C. Gonzalez, M. Head-Gordon, E.S. Replogle, J.A. Pople, Gaussian 03, (Revision C.02), Gaussian, Inc.: Wallingford, CT, 2004. http://www.gaussian.com/

[17] S.K. Wolff, D.J. Grimwood, J.J. McKinnon, M.J. Turner, D. Jayatilaka, M.A. Spackman; Crystal Explorer (2012). The University of Western Australia, Australia. https://crystalexplorer.scb.uwa.edu.au/

[18] J. J. McKinnon, M.A. Spackman, A.S. Mitchell; Acta Cryst. B 60 (2004) 627.

[19] M. A. Spackman, D. Jayatilaka, Cryst Eng Comm. 11 (2009) 249.

[20] A.L. Rohl, M. Moret, W. Kaminsky, K. Claborn, J. J. McKinnon, B. Kahr: Cryst. Growth Des. 8 (2008) 4517.

[21] M. A. Spackman, D. Jayatilaka; Cryst Eng. Comm. 11 (2009) 19.

[22] M. A. Spackmann, J.J. McKinnon, D. Jayatilaka; Cryst. Eng. Comm. 10 (2008) 377.

[23] H. Alyar, Z. Kantarci, M. Bahat, E. Kasap, Journal of Molecular Structure. 516 (2007) 34.

[24] I. Dhouib, A. Ouasri, Z. Elaoud, Journal of Chemical Saudi Society. 24 (2020) 567.

[25] A. Ouasri, A. Rhandour, M.-C Dhamelincourt, P. Dhamelincourt, A. Mazzah, M. Taibi, Journal of Raman Spectroscopy. 33 (2002) 715.

[26] A. Ouasri, A. Rhandour, M.-C Dhamelincourt, P. Dhamelincourt, A. Mazzah, M. Taibi, Journal of Phase transitions. 76 (2003) 701.

[27] F. Hlel, A. Rheim, T. Guerfel, K. Guidara, Journal of Zeitschrift fur Naturforschung Section B. 61 (2006) 1002.

[28] A. Ouasri, A. Rhandour, M. C. Dhamelincourt, P. Dhamelincourt, A. Mazzah, Journal of Spectrochimica Acta Part. A 58 (2002) 2779.
[29] A. Ben Rhaiem, F. Hlel, K. Guidara, M. Gargouri, Journal of Spectrochimica Acta Part. A 66 (2007) 1107.
[30] M. Gośniowska, Z. Ciunik, G. Bator, R. Jakubas, J. Baran, Journal of Molecular Structure. 555 (2000) 243.
[31] N. Hannachi, K. Guidara, A. Bulou, M. Gargouri, F. Hlel, Journal of Spectrochimica Acta Part. A 77 (2010) 457.
[32] J. Baran, M. Drozed, T. Lis, M. S´ ledz´, A.J. Barenes, H. Ratajczak, Journal of Molecular structure. 372 (1995) 29.

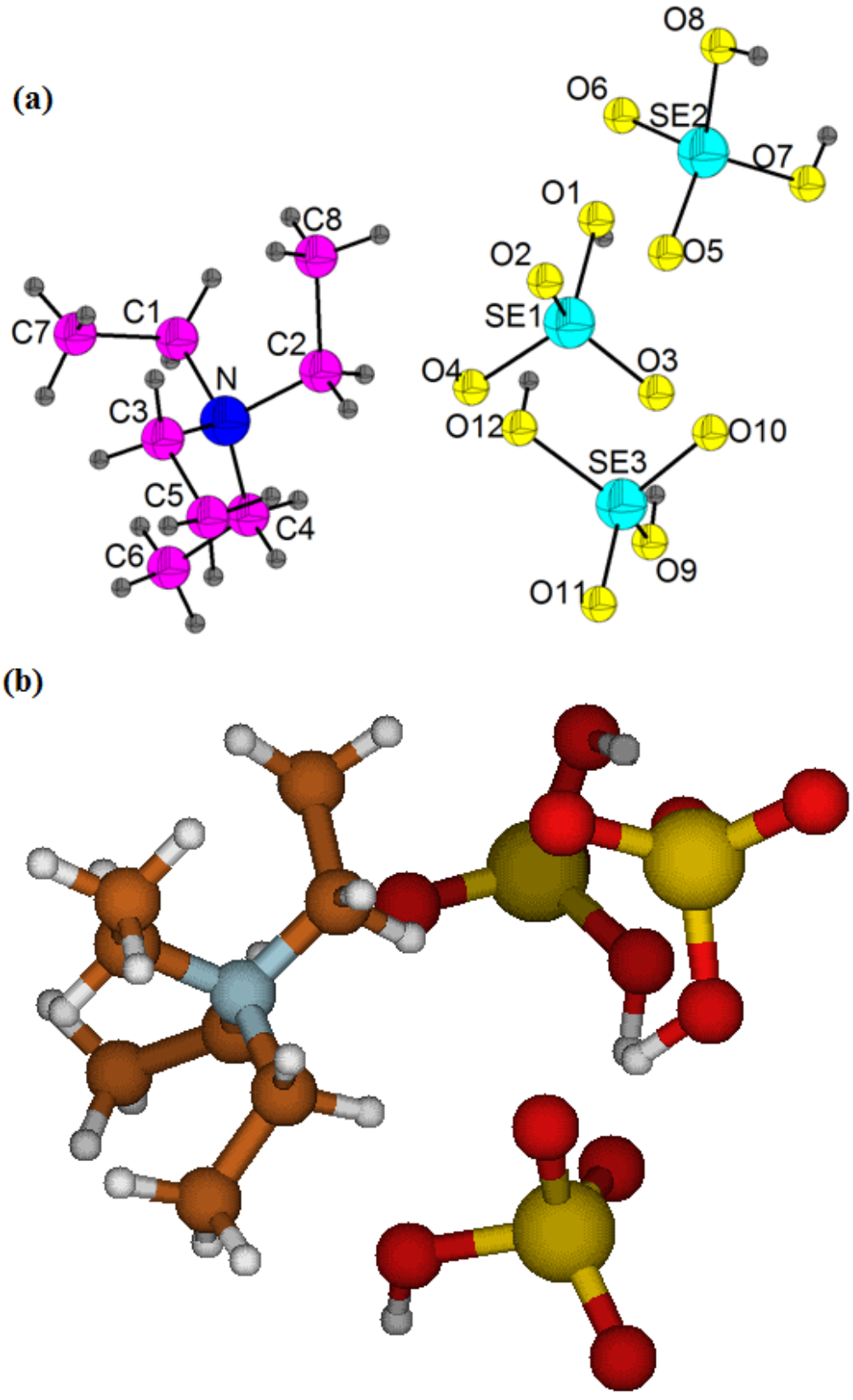

Figure 1: (a) Asymmetric unit (b) B3LYP /6-31G(d) optimized geometry of

$N(C_2H_5)_4[HSeO_4][H_2SeO_4]_2$

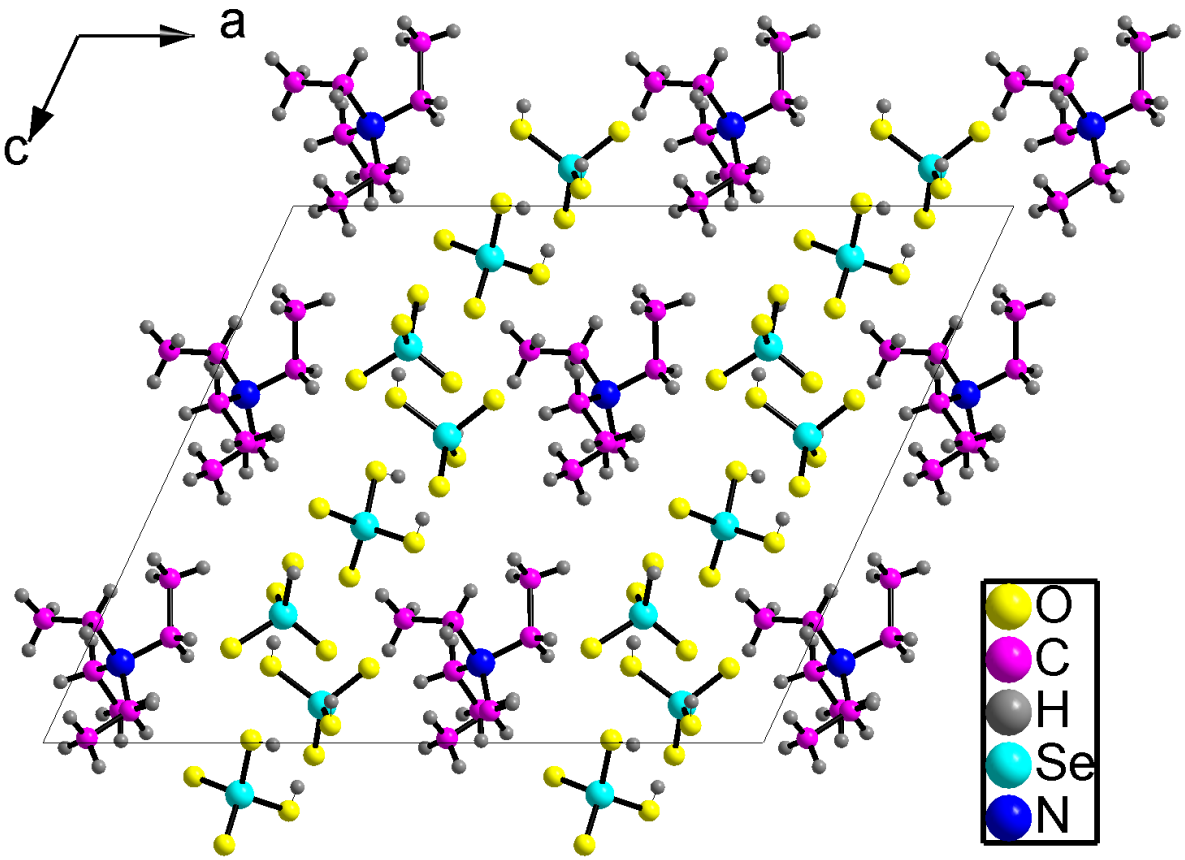

Figure 2: Projection of $N(C_2H_5)_4[HSeO_4][H_2SeO_4]_2$ structure along the crystallographic b axis

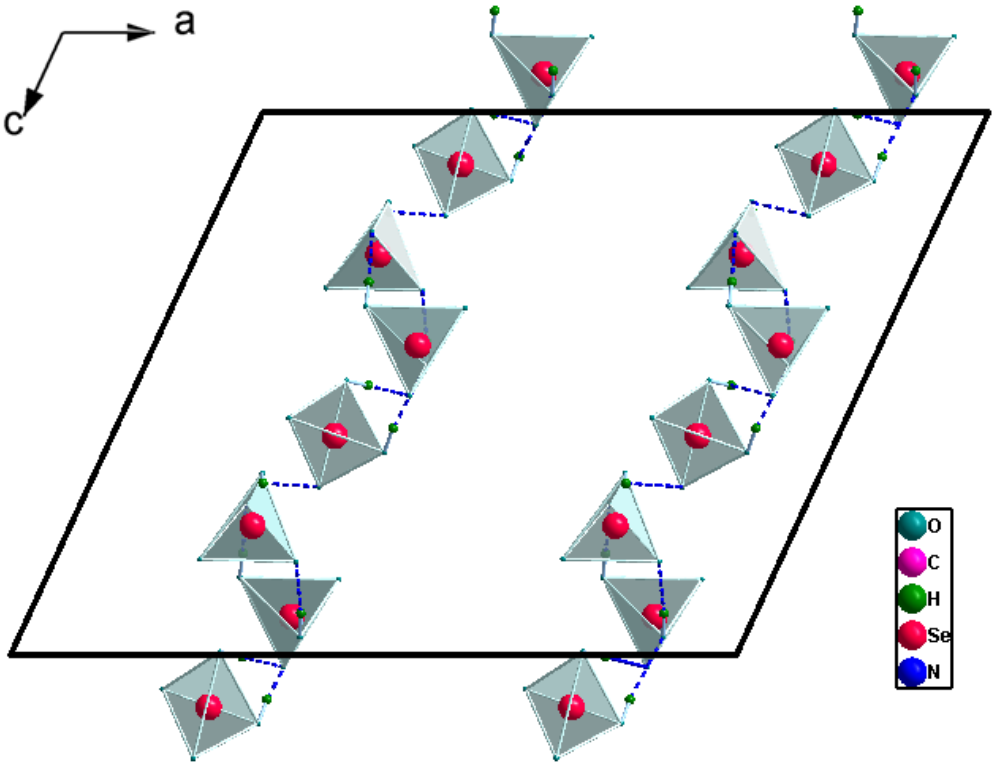

Figure 3: Projection of inorganic group structure along the crystallographic b axis

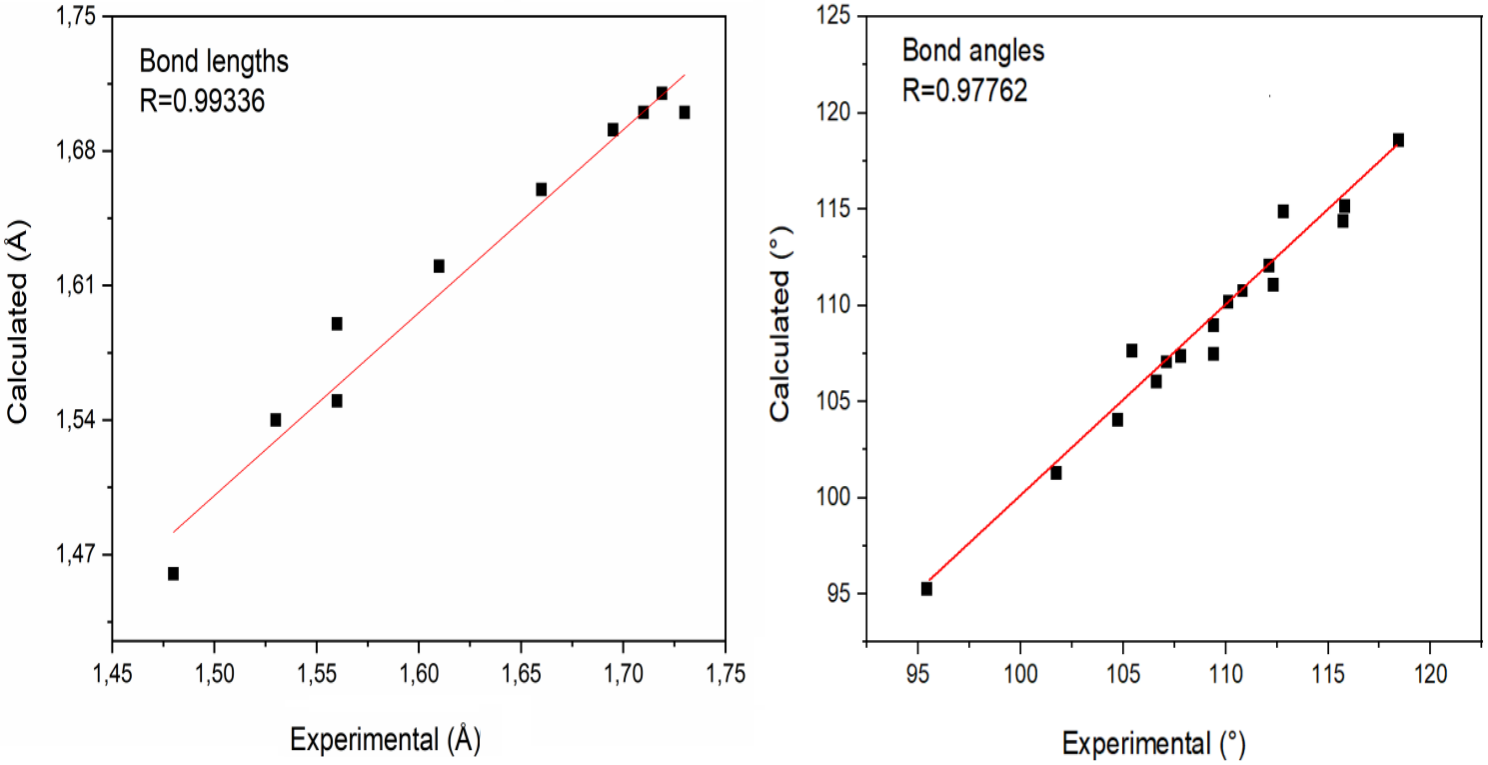

Figure 4: Correlation diagrams between experimental and calculated values for bond lengths and bond angles of $N(C_2H_5)_4[HSeO_4][H_2SeO_4]_2$ compound

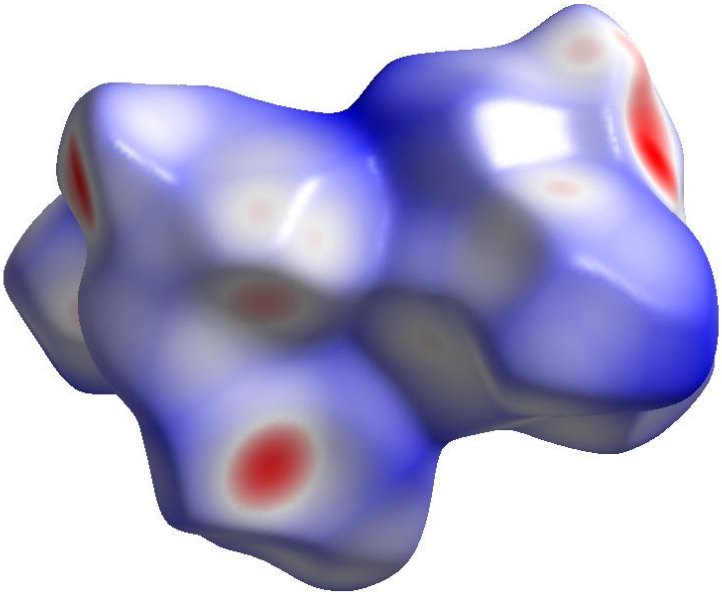

(a)

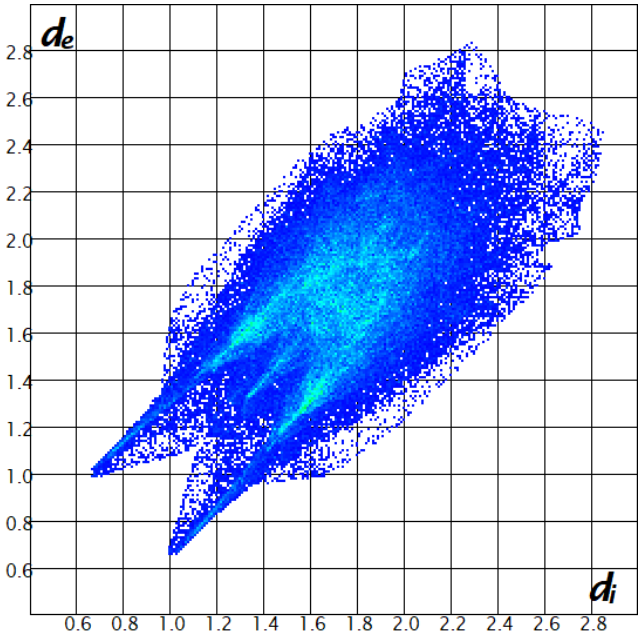

(b)

Figure 5: (a) Hirshfeld surfaces views of the $N(C_2H_5)_4[HSeO_4][H_2SeO_4]_2$ compound mapped with d_{norm}, (b) Fingerprint plot of all interactions present in the crystal packing of $N(C_2H_5)_4[HSeO_4][H_2SeO_4]_2$.

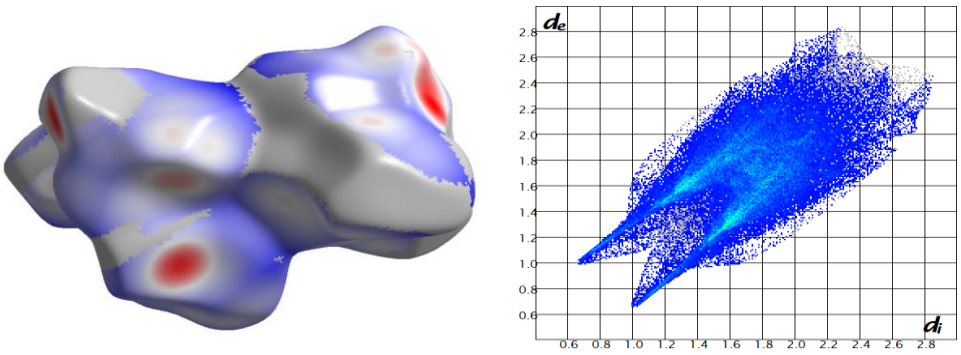

(a) : O…H/H…O (69.8%)

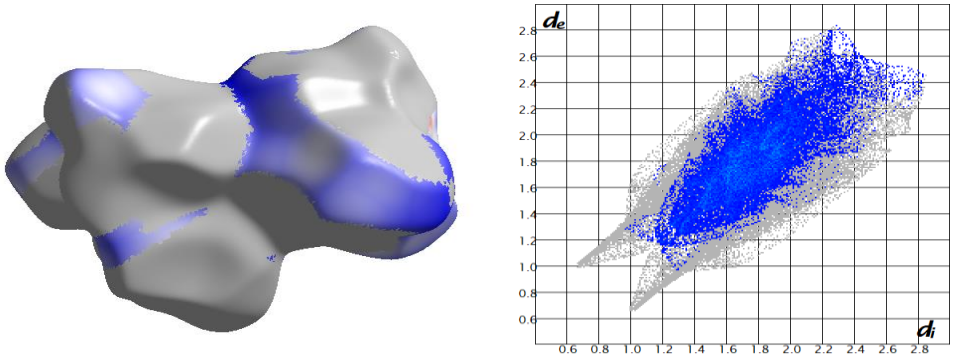

(b): H-H/H-H (25.4%)

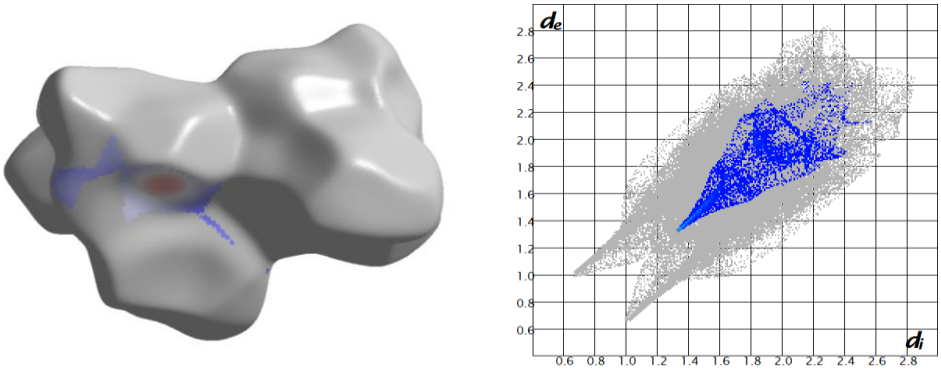

(c): O…O/O…O (4.6%)

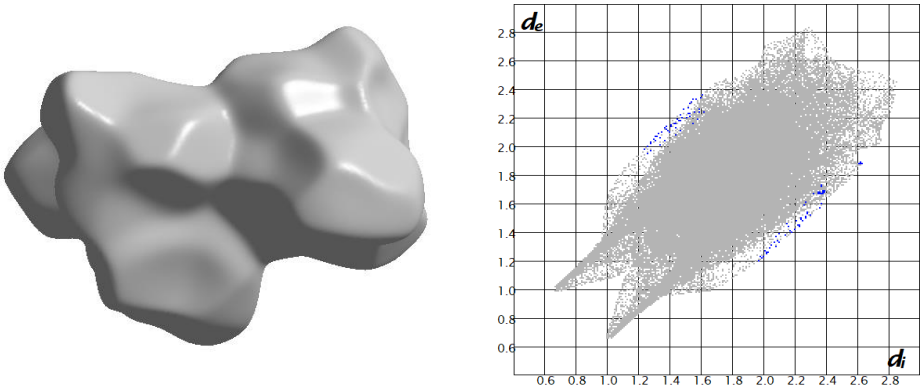

(d): Se-H/H-Se (0.1%)

Figure 6: The d_{norm} Hirshfeld surfaces and the corresponding Fingerprint plots showing the different interactions in the $N(C_2H_5)_4[HSeO_4][H_2SeO_4]_2$ crystal packing, (a): O···H/H…O, (b): H···H, (c): O···O, (d): Se···H/H···Se.

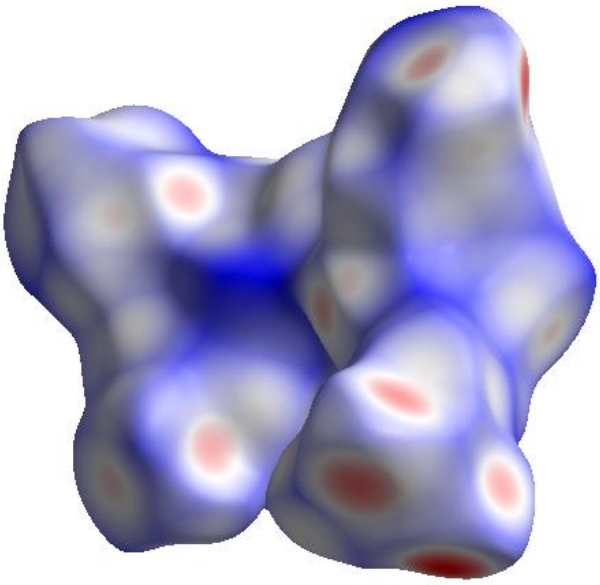

(a)

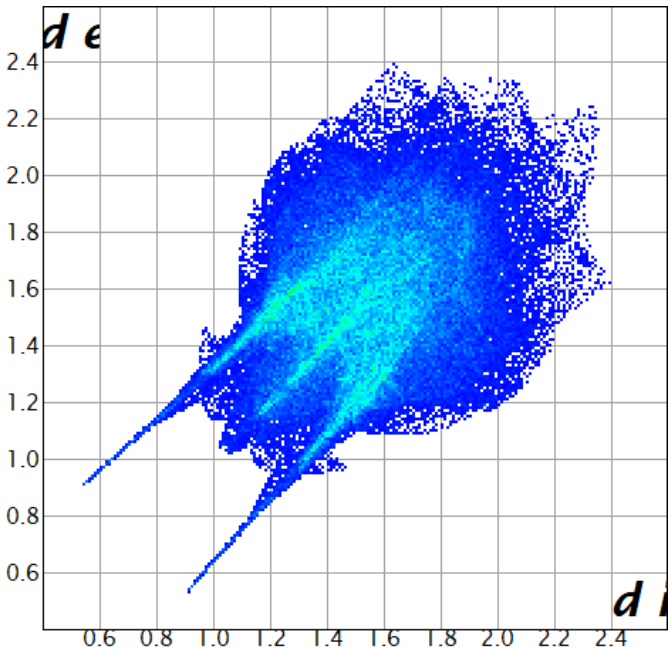

(b)

Figure 7: (a) Hirshfeld surfaces views of the $N(C_3H_7)_4[HSeO_4][H_2SeO_4]_2$ compound mapped with d_{norm}, (b) Fingerprint plot of all interactions present in the crystal packing of $N(C_3H_7)_4[HSeO_4][H_2SeO_4]_2$.

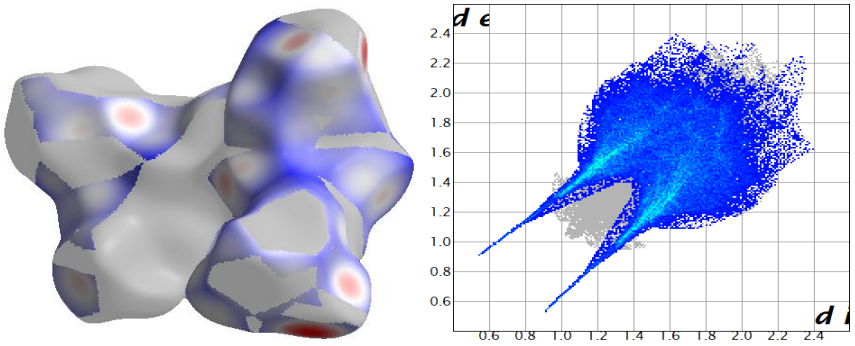

(a): O…H/H…O (56 %)

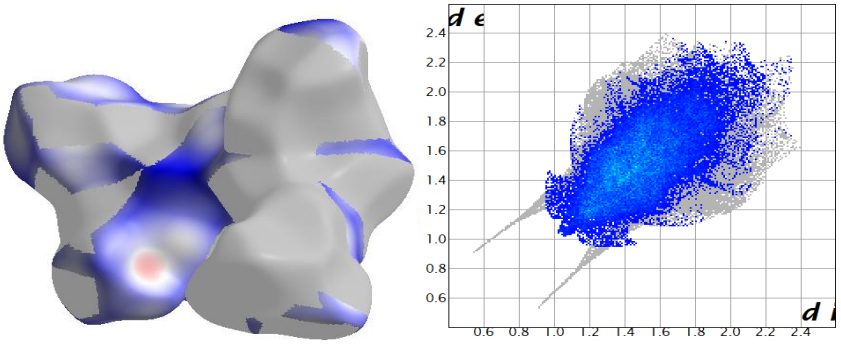

(b): H…H/H…H (36 %)

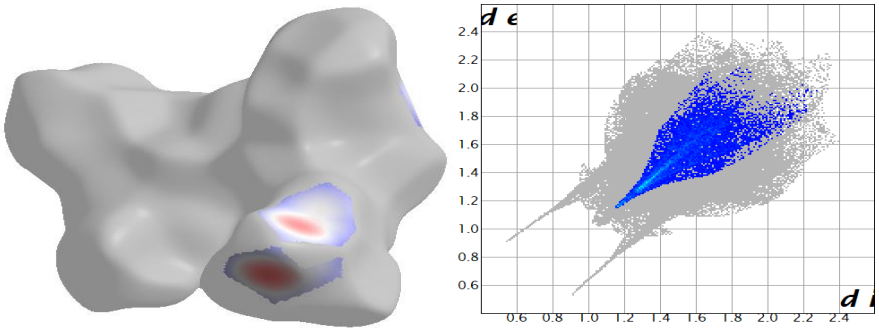

(c): O…O/O…O (7.8 %)

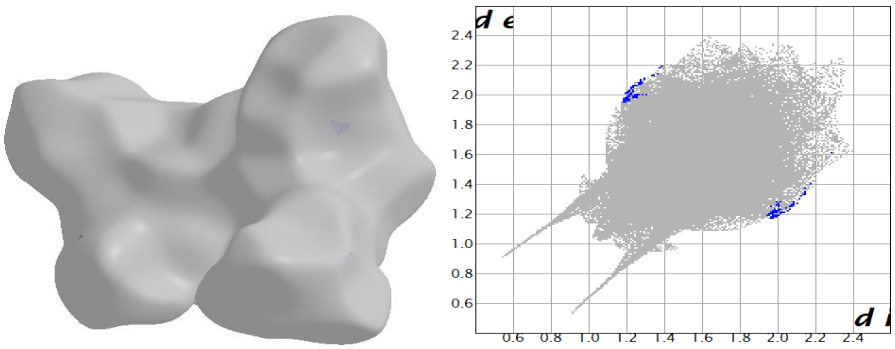

(d): Se…H/H…Se (0.1 %)

Figure 8: The d_{norm} Hirshfeld surfaces and the corresponding Fingerprint plots showing the different interactions in the $N(C_3H_7)_4[HSeO_4][H_2SeO_4]_2$ crystal packing, (a): O···H/H…O, (b): H···H, (c): O···O, (d): Se···H/H···Se.

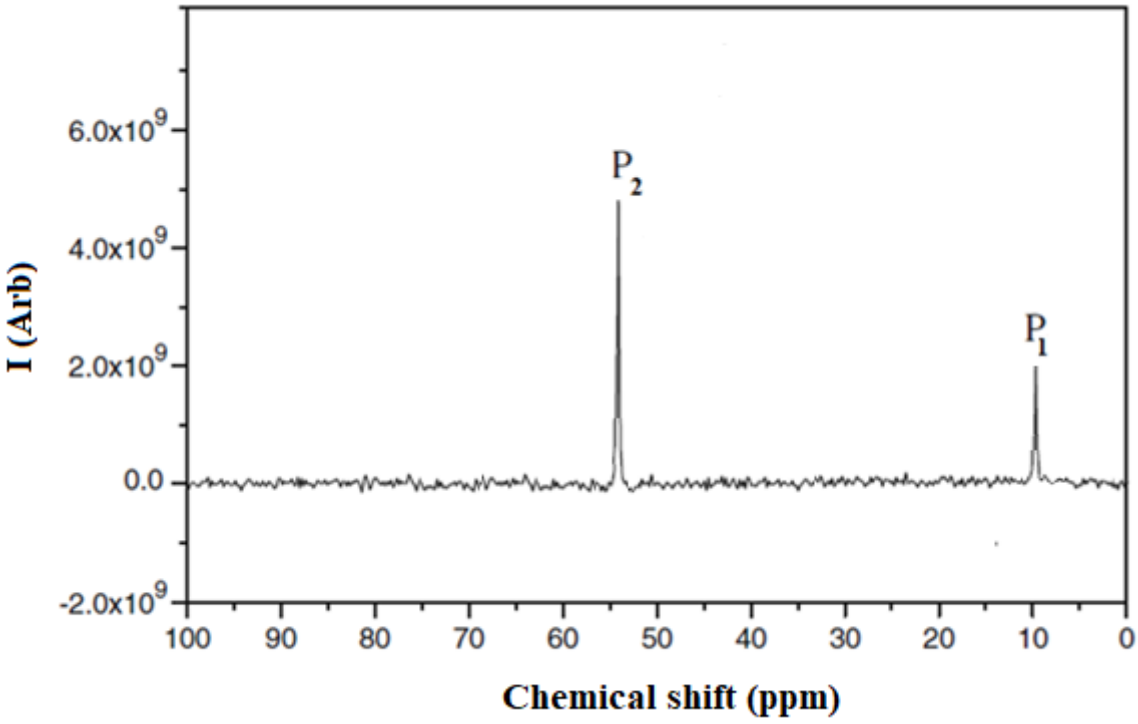

Figure 9: ^{13}C CP–MAS–NMR spectrum of $N(C_2H_5)_4[HSeO_4][H_2SeO_4]_2$

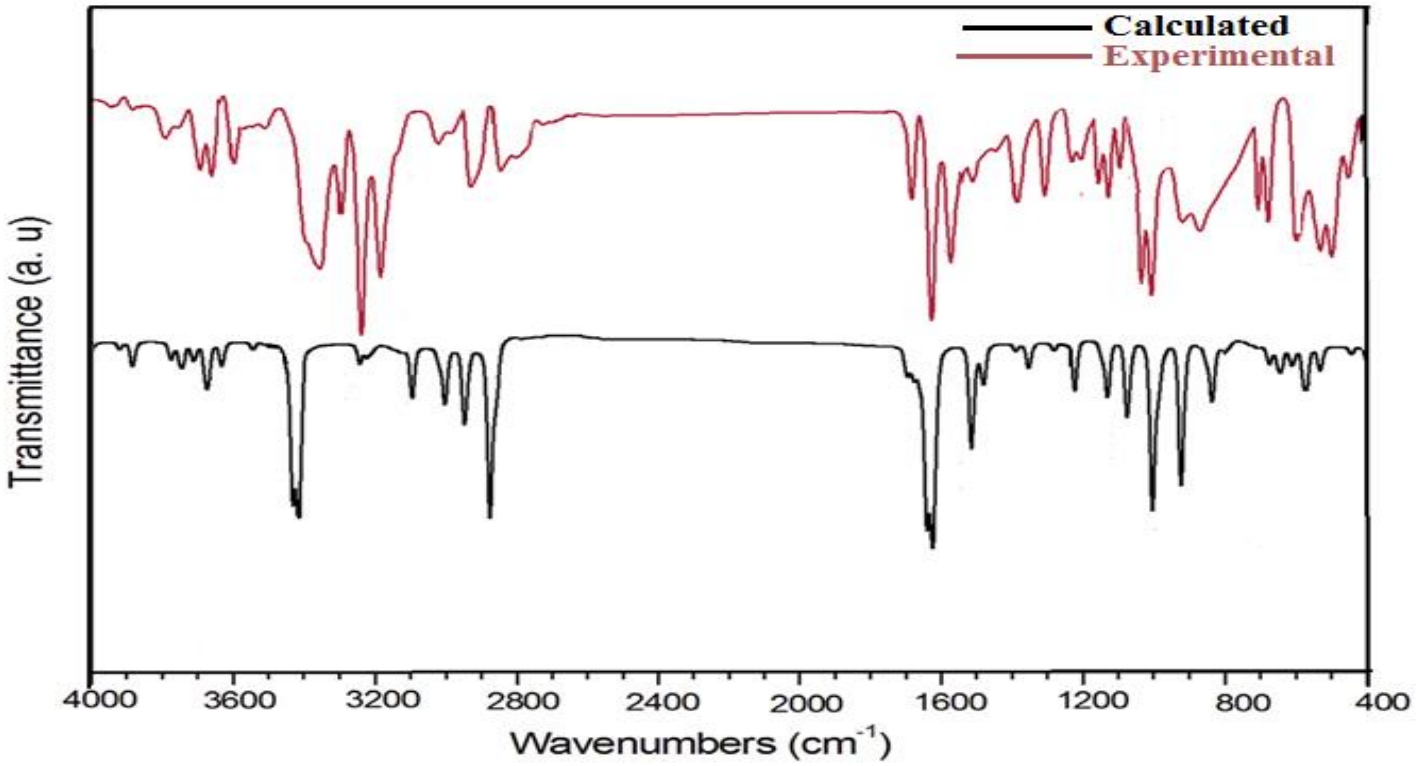

Figure 10: Superposition of (red) the experimental and (black) the DFT computed IR spectra of $N(C_2H_5)_4[HSeO_4][H_2SeO_4]_2$ in the region 400–4000 cm^{-1}

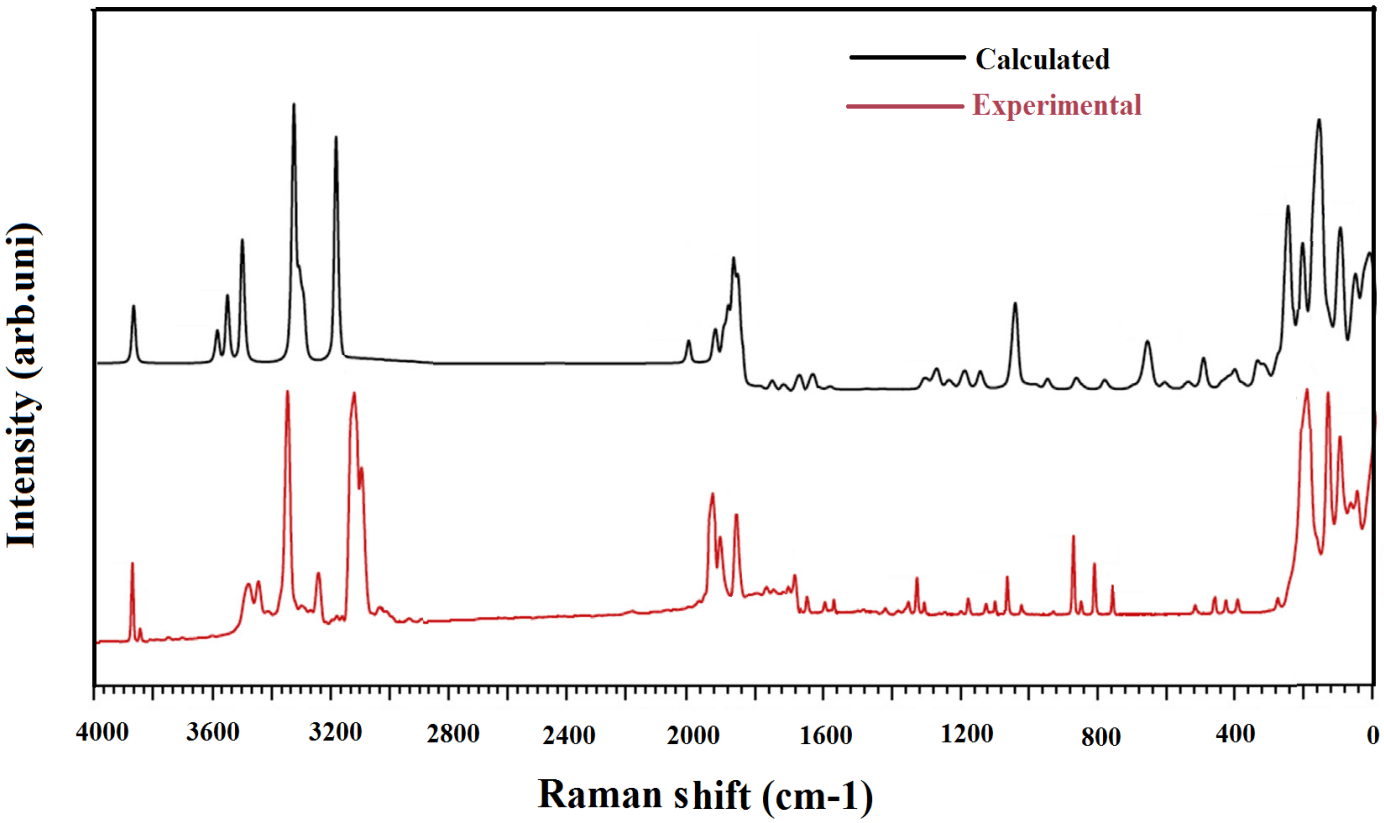

Figure 11: Superposition of (red) the experimental and (black) the DFT computed Raman spectra of $N(C_2H_5)_4[HSeO_4][H_2SeO_4]_2$ in the region 0–4000 cm^{-1}

Table 1: Comparison between the optimized geometrical parameters and the corresponding experimental data of organic part $(CH_3CH_2)_4N$.

Parameters	**Observed**	**Calculated**
Bond length (Å)		**B3LYP/6-31G(d)**
N-C1	1.64(2)	1.59
N-C2	1.56(1)	1.54
N-C3	1.48(1)	1.53
N-C4	1.53(2)	1.53
C1-C7	1.61(2)	1.56
C2-C8	1.66(1)	1.61
C3-C5	1.56 (1)	1.54
C4-C6	1.50(1)	1.53
N-C7-C1	95.4(9)	96 .5
N-C2-C8	118.4(10)	117.14
N-C3-C5	110.8(10)	110.1
N-C4 -C6	110.8 (6)	111.2
C2-N-C1	101.4(11)	102.3
C3-N-C1	110.7(12)	107.2
C3-N-C2	110.1(12)	109.8
C4-N-C1	112.8 (12)	111.9
C4-N-C2	109.4(10)	108.7
C4-N-C3	111.9(12)	111.5

Table 2: Comparison between the optimized geometrical parameters and the corresponding experimental data of inorganic part $(HSeO_4^-)(H_2SeO_4)_2$.

Parameters	**Observed**	**Calculated**
Bond length (Å)		**B3LYP/6-31G(d)**
Se1-O1	1.824(12)	1.83
Se1-O2	1.703(14)	1.69
Se1-O3	1.549(13)	1.61
Se1- O4	1.766(7)	1.71
O1-Se1-O2	107.8 (5)	108.8
O1-Se1- O3	106.6(6)	106.4
O2-Se1-O3	115.8(6)	114.6
O1-Se1-O4	109.4(6)	109.4
O2-Se1-O4	112.3 (5)	112.53
O3-Se1-O4	104.7 (5)	104.3
Se2-O5	1.719 (9)	1.79
Se2 -O6	1.695 (10)	1.69
Se2- O7	1.730 (9)	1.70
Se2- O8	1.784 (14)	1.79
O8- Se2- O6	101.7(6)	98.07
O8- Se2-O7	112.1(6)	111.4
O6- Se2-O7	107.1(5)	108.53
O8- Se2-O5	115.7(6)	114.6
O6- Se2- O5	112.8(6)	112.3
O7- Se2-O5	107.2(5)	106.62
Se3- O9	1.723(10)	1.73
Se3- O10	1.688(8)	1.67
Se3- O11	1.718(7)	1.70
Se3- O12	1.774(11)	1.71
O11- Se3-O12	108.3(5)	107.4
O11- Se3- O10	114.7(4)	113.9
O12- Se3-O10	102.4(5)	101.5
O11- Se3-O9	108.7(5)	107.6
O12- Se3- O9	113.4(3)	112.9
O10- Se3- O9	109.3(5)	108.78

Table 3: Important contacts and their characteristic distances (de, di) in the crystal packing of the two selenate compounds

Compound	O….H/H…O	H….H/H…H	O….O/O…O	Se….H/H…Se
$N(C_2H_5)_4[HSeO_4][H_2SeO_4]_2$				
Occupation area	69.8 %	25.4 %	4.6 %	0.1 %
Donor (de, di) **Acceptor (de, di)**	(1 Å, 0.68 Å) (0.68 Å, 1Å)	(1.2 Å, 1.2 Å)	(1.3 Å, 1.3 Å)	……
$N(C_3H_7)_4[HSeO_4][H_2SeO_4]_2$				
Occupation area	56 %	36 %	7.8 %	0.1 %
Donor (de, di) **Acceptor (de, di)**	(0.92 Å, 0.54 Å) (0.54 Å, 0.92 Å)	(1.05 Å, 1.05 Å)	(1.17 Å, 1.17 Å)	……

Table 4: The electric dipole moment μ_{tot} (D), the polarizability α ($\times 10^{-24}$ ues) and the first hyperpolarizability β ($\times 10^{-31}$ ues) of $N(C_2H_5)_4[HSeO_4]$ $[H_2SeO_4]_2$ computed using DFT//B3LYP/6-31G(d)

μx	12.6018	βxxx	77.9620
μy	-4.2282	βyyy	-119.2789
μz	1.7615	βzzz	-32.4468
μ	**13.4084**	βxyy	-54.3456
αxx	34.1055	βxxy	-42.1829
αyy	-18.6620	βxxz	36.0127
αzz	-15.4435	βxzz	-29.6624
αxy	2.0642	βyzz	25.2862
αxz	4.8480	βyyz	-31.7380
αyz	-11.0030	βxyz	34.0793
αtot	**0**	**βtot**	**12.0259**

Table 5: Correlation diagram of internal vibration modes of $(CH_3CH_2)_4N^+$ (D_{2d}--- C_1 --- C_s)

Point Group $\mathbf{D_{2d}}$	Site Group $\mathbf{C_1}$	Factor Group $\mathbf{C_s}$
12 A_1 (Ra)		
8 A_2 (IR)		
9 B_1 (Ra)	81A (Ra, IR)	81A’ (Ra, IR)
12 B_2 (IR)		81 A”(Ra, IR)
20 E (Ra, IR)		

Table 6: Correlation diagram of internal vibration modes of H_2SeO_4 group (C_{2v}--- C_1 --- C_s)

Point Group $\mathbf{C_{2v}}$	Site Group $\mathbf{C_1}$	Factor Group $\mathbf{C_s}$
6 A_1 (Ra, IR) 4 B_1 (Ra, IR) 2 A_2 (Ra) 3 B_2 (Ra, IR)	15 A (IR, Ra)	15 A'(IR, Ra) 15 A''(IR, Ra)

Table 7: Diagram correlation of internal vibration modes of $[HSeO_4]^-$ group (C_{3v} --- C_1 --- C_s)

Molecular Group $\mathbf{C_{3v}}$	Site Group $\mathbf{C_1}$	Factor Group $\mathbf{C_s}$
4 A_1 (Ra, IR) 2 A_2 (Ra) 3 E (Ra, IR)	12 A (IR, Ra)	12A'(IR, Ra) 12 A''(IR, Ra)

Table 8: The vibrational modes representation of $[(H_2SeO_4)_2HSeO_4]^-$ in the crystal.

Species	SeO_4^{2-} modes in		OH modes in
	T_d symmetry	C_1 symmetry	C_1 symmetry
$2 \times (H_2SeO_4)$	$2A_1 + 2E + 4F_2$	18 A	12A
$[HSeO_4]^-$	$3A_1 + 3E$	9 A	3 A
$[(H_2SeO_4)_2HSeO_4]^-$	$5A_1 + 5E + 4F_2$	27 A	15 A

Table 9: The observed and calculated frequencies (cm^{-1}) of $[(C_2H_5)_4N]HSeO_4(H_2SeO_4)_2$

Observed		Calculated B3LYP/6-31G*		Assignment
IR	**Raman**	**IR**	**Raman**	
3935 vw 3876 vw 3789 w 3740 sh	3875 m 3850 vw	3915 vw 3873 w 3768 vw 3736 vw	3878 m	ν (Se-OH)
3695 w 3663 w 3600 w		3705 vw 3684 w 3620 w	3600 w	ν (Se-OH)
3500 vw		3536 vw		ν (Se-OH)
	3475 w 3450 w		3500 m	ν (OH…O)
3370 s, b	3350 s	3410 s	3340 s	ν (OH…O)
3315 m				ν (OH…O)
3242 s 3200 s	3238 w 3125 s	3248 vw ----	---- 3175 s	ν (OH…O) / ν (OH)
	3100 s		----	ν (OH…O)
3030 w	3025 w	3010 m	----	$\nu_{as}(CH_3)$ / $\nu_{as}(CH_2)$
3000 vw		----		$\nu_{as}(CH_3)$ / $\nu_{as}(CH_2)$
2937 m		2957 m		$\nu_s(CH_2)$ / $\nu_s(CH_3)$
2863 m		2884 s		$\nu_s(CH_2)/\nu_s(CH_3)$ / ν (OH----O)
2800 w, b				ν (OH----O)
	1935 m 1903 m 1860 m 1772 vw		1930 w 1892 w 1881 m 1770 w	Non fundamental modes
1684 m	1686 w	1695 w	1670 w	δ (Se-OH)
1642 s 1600 m	1654 w 1600 vw	1652 s 1620 s	1633 w	δ (Se-OH)
	1568 w		1578 vw	δ (Se-OH)
1516 w		1516 m		δ (Se-OH) / $\delta_{as}(CH_3)/\delta_{as}(CH_2)$
1453 w		1473 w		$\delta_{as}(CH_3)$ / $\delta_{as}(CH_2)$
1410 m	1410 vw	1412 vw	----	$\delta_s(CH_3)$ / $\delta_s(CH_2)$
	1358 w		----	$\delta_s(CH_3)$ / $\delta_s(CH_2)$
	1326 m		1315 w	t (CH_2)
1305m	1305 vw	1285 w	1285 w	t (CH_2) / δ (OH)
1242 m		1232 m		$\rho_r(CH_3)$
1200 m		----		$\rho_r(CH_3)$
1168 m	1168 w	---	1178 w	ν_{as} (C-N) / ν_{as} (C-C) / $\rho_r(CH_3)$
1137 m		1135 m		ν_{as} (C-N) / ν_{as} (C-C) / $\rho_r(CH_3)$
	1116 w		1130 w	ν_{as} (C-N) / ν_{as} (C-C) / $\rho_r(CH_3)$
1105 w	1095 vw	1095 m	----	γ (Se-OH)
1053 s	1053 m	-----	1032 m	γ (Se-OH)
1030 s		1021 s		γ (Se-OH)

	1010 w		-----	γ (Se-OH)
947 m		936 s		ν_3 [ν_{as} (Se-O)]
905 m		-----		ν_3 [ν_{as} (Se-O)]
	874 m		-----	ν_3 [ν_{as} (Se-O)]
	842 w		863 w	ν_1 [ν_s (Se-O)]
	800 m		780 w	ν (Se–OH)
	748 m		----	ν (Se–OH) / ν_s (C-N)/ν_s C-C)
727 m		----		ν (Se–OH) / ν_s (C-N)/ν_s C-C)
674 m		675 w		ν_s (C-N) / ν_s C-C)
632 m		635 w		ν_s (C-N) / ν_s C-C)
547 m		546 w		δ_{as} (N-C-C) / δ_{as} (C-C-C)
	516 w		505 m	ν_4 (δ_{as} : O-Se-O)
453 w	463 w	444 w	----	ν_4 (δ_{as} : O-Se-O)
	421 w		----	ν_4 (δ_{as} : O-Se-O)
	400 w		402 w	ν_4 (δ_{as} : O-Se-O)
	274 w		263 s	ν_2 (δ_s : O-Se-O)
	211 s		221 m	------
	147 s		158 s	-----
	105 s 63 vw 42 w		103 s 45 w	Lattice modes

s: strong, m: medium, w: weak, vw: very weak, b: broad, sh: shoulder